**Atmospheric
Measurement
Techniques**
Open Access
Discussions

A novel algorithm for detection of precipitation in tropical regions using PMW radiometers

D. Casella, G. Panegrossi, P. Sanò, L. Milani, M. Petracca, and S. Dietrich

Consiglio Nazionale delle Ricerche – Istituto di Scienze dell'Atmosfera e Del Clima (CNR-ISAC), Rome, Italy

Correspondence to: D. Casella (daniele.casella@artov.isac.cnr.it)

Abstract

A novel algorithm for the detection of precipitation is described and tested. The algorithm is applicable to any modern passive microwave radiometer on board polar satellites independently of the observation geometry and channel frequency assortment. The algorithm is based on the application of canonical correlation analysis (CCA) and on the definition of a threshold to be applied to the resulting linear combination of the brightness temperatures in all available channels. The algorithm has been developed using a two-year dataset of co-located SSMIS and TRMM-PR measurements and AMSU-MHS and TRMM-PR measurements. This dataset was partitioned into 4 classes depending on the background surface emissivity (vegetated land, arid land, ocean, and coast) and the same procedure was applied for each surface class. In this paper we describe the procedure and we evaluate the results in comparison with many well-known algorithm for the detection of precipitation.

The novel CCA algorithm show a small rate of false alarms and superior detection capability, it can efficiently detect (POD between 0.53 and 0.70) minimum rain rate varying from $0.15\,\mathrm{mm\,h^{-1}}$ (AMSU over ocean) to 0.40 (SSMIS over coast) with the remarkable result of $0.23\,\mathrm{mm\,h^{-1}}$ over arid land surface. The total amount of precipitation that the CCA algorithm can detect is around 80 % over Ocean and Vegetated land and between 68 and 75 % over coast and arid land.

1 Introduction

The Global Precipitation Measuring mission (GPM) (Hou et al., 2014) started its operational phase on 28 February 2014, with the launch of the NASA/JAXA GPM Core Observatory. The goal of the mission is to provide *globally* instantaneous precipitation measurements with a coverage of less than 1 h in 60 % of the globe and less than 3 h in the 80 % of the globe by 2015, through the exploitation of a constellation of passive microwave (PMW) radiometers onboard research and operational satellites provided

by the United States, Japan, France, India, and the European Community. The GPM Core Observatory carries the first spaceborne dual-frequency precipitation radar, the Dual Polarization Radar (DPR), operating at Ku and Ka bands (13 and 35 GHz, respectively) and a conical-scanning multi-channel (10–183 GHz) microwave imager, the GPM Microwave Imager (GMI). The GPM constellation consists of radiometers with different scanning geometry (both conical scanning and cross-track), different assortment of multichannel frequencies and polarization, and different spatial resolution. The microwave imagers and sounders with a conical scanning observation geometry are: (1) Special Sensor Microwave Imager/Sounder (SSMIS) measures microwave energy at 24 discrete frequencies from 19–183 GHz (Kunkee et al., 2008). (2) Advanced Microwave Scanning Radiometer 2 (AMSR-2) (Shimoda, 2005) with channels ranging from 6.9–89 GHz. (3) Sounder for Probing Vertical Profiles of Humidity (SAPHIR) with 6 channels in the 183 GHz water vapor absorption band, the last two instruments carried by the French-Indian satellite Megha-Tropique (Desbois et al., 2003). The cross track scanners are: (1) the Mirowave Humidity Sounder (MHS) (89–190 GHz) onboard the NOAA Polar Orbiting Environmental Satellites (POES) satellites and on the EU-METSAT MetOp satellites (Edwards and Pawlak, 2000). (2) The Advanced Technology Microwave Sounder (ATMS) instrument on the NPOESS NPP satellite and on the NOAA–NASA JPSS satellites (Muth et al., 2005) with 22 channels in the range of frequency 23.8–183 GHz. It is worth mentioning also the Advanced Microwave Sounding Unit-A (AMSU-A) which is another cross track scanner with 15 channels ranging from 23.8–89 GHz; this last instrument is not included in the official GPM constellation, however it is carried by the same satellites equipped with the MHS radiometer.

Obtaining coherent (and accurate) precipitation estimates from this assortment of instruments requires a robust inter calibration of the brightness temperatures (TBs). The GPM has established an international team called Intersatellite Calibration Working Group (X-CAL) in order to address this need (Wilheit, 2013). Moreover the estimates themselves need to be obtained with common procedures and datasets. The 2014 version of the Goddard Profiling Bayesian algorithm (GPROF2014) (Kummerow et al.,

Title Page

Abstract | Introduction

Conclusions | References

Tables | Figures

◀ | ▶

◀ | ▶

Back | Close

Full Screen / Esc

Printer-friendly Version

Interactive Discussion

2001, 2011) will be applied to all passive microwave radiometers in the GPM constellation and will be the official NASA PMW precipitation retrieval algorithm for GPM.

However also achieving consistency in the detection of precipitation among the different radiometers is of primary importance. This can be accomplished by developing common procedures to be applied to all the different radiometers able to detect efficiently the presence of precipitation in different environmental conditions. Consistency and accuracy are also the priorities in the development of our PMW precipitation retrieval algorithms used for the operational PMW precipitation products within the EU-METSAT "Satellite Application Facility on Support to Operational Hydrology and Water Management" (H-SAF) program (see Mugnai et al., 2013a). The H-SAF PMW algorithms for cross-track and conical scanning radiometers are built upon the same physical foundations and use common procedures for the detection of the precipitation (see Casella et al., 2013; Sanò et al., 2013, 2014; Mugnai et al., 2013b; Panegrossi et al., 2013).

Detection of precipitation from satellite using passive microwave radiometers is a difficult task, since the brightness temperatures emerging from precipitating clouds can be similar to the ones emitted by some type of surface in clear sky conditions. Precipitation detection is simpler over ocean, because in the low frequency channels (10–30 GHz) the surface background appears relatively cold (in terms of brightness temperature), due to the low and nearly uniform sea surface emissivity and this allows to detect the absorption/emission from large rain drops as relatively warm areas. Over land the detection of precipitation is more complex as the rain layers emission is obscured by the high emissivity of the background surface. The detection of precipitation has still some open issues (see Munchak and Skofronick-Jackson, 2013) especially over coast, arid regions, and over snow covered surfaces. It is worth noting that some algorithms for precipitation estimate do not include specific procedures for the detection of precipitation and provide just a "probability of precipitation" (e.g. GPROF from version 7 of the TMI-GPROF and in the GMI-GPROF; GPM, 2010). However an accurate procedure for the detection of precipitation could be very useful within the algorithms estimat-

Title Page

Abstract   Introduction

Conclusions   References

Tables   Figures

◀   ▶

◀   ▶

Back   Close

Full Screen / Esc

Printer-friendly Version

Interactive Discussion

ing precipitation in order to separate the problem of identifying the precipitating areas from the problem of estimating the intensity of the rainfall. Moreover in the regions of the Earth were precipitation is unfrequent (e.g. in semi-arid regions in the tropics) precipitation detection is crucial for drought monitoring. As a matter of fact, over the last twenty years, different precipitation detection procedures have been widely used within precipitation retrieval algorithms.

It is quite common in the framework of precipitation estimate to refer to precipitation detection as "screening". Some approaches widely used are based on the scattering index (SI) over land surface (i.e. Grody, 1991; Ferraro, 1997). Another classical approach makes use of the polarization corrected temperatures (Spencer et al., 1989; Barrett et al., 1988; PCT). Unfortunately these algorithms cannot be applied to the cross-track scanning radiometers (e.g. AMSU-A, AMSU-B, MHS, ATMS), because they need both vertical and horizontal polarized channels at the same frequency. However the most recent spaceborne radiometers utilize high frequency channels (150–160 GHz), and sounding channels in the 60 GHz oxygen absorption band and in the 183 GHz water vapor absorption band. As a consequence relatively new algorithms for the detection of precipitation have been developed (e.g. Chen and Staelin (2003), that uses both the 52.3 GHz channel and the 183 GHz channels and Laviola and Levizzani (2011) that make large use of the water vapor absorption band channels around 183 GHz). Recently more efforts have been made in solving the detection of precipitation issue: among others Grecu and Anagnostou (2001) had applied a neural network approach, Seto et al. (2005) have developed a lookup-database method, Laviola and Levizzani (2009) proposed a simple technique based upon a threshold on an AMSU-B channel combination, Islam et al. (2014) have built a random forest classifier.

In this paper we will describe a novel precipitation screening algorithm based on Canonical Correlation Analysis (CCA). The novelty of the algorithm is that it is applicable to all available PMW radiometers in the GPM constellation, it is in principle very simple, and it is conditioned to the availability of a large dataset of co-located measurements of multi-channels TBs and high quality precipitation measurements. The

A novel algorithm for detection of precipitation in tropical regions

D. Casella et al.

Title Page

Abstract	Introduction
Conclusions	References
Tables	Figures

|◄ | ►|

◄ | ►

Back | Close

Full Screen / Esc

Printer-friendly Version

Interactive Discussion

algorithm was inspired by the approach of Petty (2013), who developed a methodology based on a two-stage principal component analysis finalized to reducing the dimensionality of the input in a Bayesian algorithm for the estimate of precipitation and in "distilling" the relevant information from a multidimensional set of channels. The approach of Petty (2013) has been modified and adapted to the problem of precipitation detection. We will show the results of our algorithm and compared them to those obtained from different well known techniques for precipitation detection. The novel CCA based algorithm described in this paper is currently applied to the PMW precipitation retrieval algorithms currently used to deliver operational products of instantaneous precipitation over Europe and African regions within the EUMETSAT H-SAF program (Mugnai et al., 2013a, b; Casella et al., 2013; Sanò et al., 2013, 2014).

This paper is divided into 5 sections. Section 2 describes the datasets of co-located measurements of multi-channels TBs (from SSMIS and AMSU/MHS) and precipitation measurements (from the Tropical Rainfall Measuring Mission (TRMM) precipitation Radar (PR)) used in the training of the novel algorithm. A description of the procedures followed to separate the dataset depending on the type of background surface and to reduce the parallax errors are also provided. Section 3 illustrates the methodology used for the definition of the algorithm. Section 4 shows the results of the application of the algorithm to the dataset described in Sect. 2 in terms of probability of detection (POD), false alarm ratio (FAR) and Heidke skill score (HSS), with variable rain/no-rain thresholds. Results of the comparisons with other screening algorithms are also provided and the performance of the novel algorithm is described in terms of minimum detectable rain and of total error for each background surface type. Finally Sect. 5 includes the summary of the main results and the conclusions.

2 Instruments and dataset description

The study was carried out in the area between 36° S–36° N in latitude and 60° E–60° W in longitude, covering the African continent, part of the Arabian Peninsula, part of the

Southern American continent and part of the Atlantic and Indian Ocean. All the analysis was performed considering coincident observations of the Tropical Rainfall Measuring Mission (TRMM) precipitation Radar (PR) with observations from SSMIS and AMSU/MHS radiometers in the years 2011 and 2012. The TRMM-PR is the first space-borne precipitation radar which has been recently declared no longer operational and can be considered the precursor of GPM DPR. It is a 13.8 GHz radar scanning between −17° and +17° with a swath width of 247 km (after the satellite was boosted at higher orbit in 2001). SSMIS is conical scanning radiometer with an observation angle of 53.1°, with a swath width of 1700 km, measuring passive microwave radiation in 24 channels with frequencies ranging from 19–183 GHz. The 19, 37 and 91 GHz channels are both in the vertical and horizontal polarization while the 22 and 150 GHz channels are present only in the horizontal polarization as the channels in the oxygen absorption band (50.3–60.8 GHz) and in the water vapor absorption band (around 183.31 GHz). The SSMIS radiometer is carried onboard 4 satellites of the Defense Meteorological Satellite Program (DMSP) the F16, F17, F18 and F19; the launch of F20 satellite is planned for 2020. AMSU-A and MHS are both cross track sensors onboard 4 satellites NOAA-18, NOAA-19, Metop A and Metop B. AMSU-A has 23 channels between 23.8 and 89 GHz while MHS has one channel at 89 GHz, one at 157 GHz and 3 channels in the water vapor absorption band. The polarization measured by every channel changes with the scan angle which varies between −48° and 48°, and the swath width of the radiometer is around 1920 km.

We selected all available coincidences (considering a 15 min time window) of the SSMIS radiometer with the TRMM PR in the area of interest considering the DMSP-F16, DMSP-F17 and DMSP-F18 satellites (i.e. the ones available in the years considered). The same was done for the available AMSU/MHS radiometers considering Metop-A, NOAA-18, and NOAA-19 satellites. Two datasets have been created, one of SSMIS-PR coincidences and one of AMSU/MHS-PR coincidences, with a total of 5247 and 2149 coincident overpasses for the AMSU/MHS and for the SSMIS dataset respectively. To obtain co-located vectors of SSMIS or AMSU/MHS brightness temperatures

(TBs) and PR rainfall estimates (TRMM product 2A25), there are important issues to be considered: the parallax error between PMW radiometers and TRMM PR, and the fact that horizontal resolution changes with frequency in conically scanning MW radiometer (SSMIS) and with the observation angle in the cross-track scanning radiometers (AMSU/MHS). Moreover there are sampling differences between AMSU-A and MHS and between the SSMIS components (Imager, Environmental, Lower and Upper Atmospheric Sounder). First a partial correction of the parallax error was carried out (shortly described below). Then, the TRMM-PR rainfall rate at the surface was downscaled to the SSMIS and MHS nominal resolution, defined as the IFOV size of the 91 GHz/89 GHz channel for the SSMIS/MHS radiometer respectively. All the channels with a coarser spatial grid were re-sampled using a nearest neighbor approach, and for the AMSU-A/MHS sensors we have considered an IFOV size variable with the scan angle as described by (Bennartz, 2000).

The resulting datasets were divided into 3 classes depending on the background surface as: Land, Ocean and Coast using a digital land/sea map at 2 s of arc resolution. Then the Land class was subdivided into Vegetated Land and Arid Land (desert). The Arid Land pixels have been identified looking at the mean annual difference of the SSMIS 19 GHz V and H channels. (Grody, 1991) has shown how the difference of the V and H polarized channels are very effective in identifying desert. Although the presence of clouds may reduce the polarization difference, this effect may be minimized by averaging the TB difference over a long period. In this study we have looked at one year (2011) of SSMIS observations over the area of interest, selecting the observations over land, and remapping them on a regular grid in latitude and longitude (with 0.5° spacing).The difference of the TBs of the 19 GHz V and H channels (dTB_{19}) was calculated for each grid point and then averaged over a year. If the mean annual difference of dTB_{19} was higher than 15 K:

$$\overline{dTB_{19}} = \overline{TB_{19V} - TB_{19H}} > 15\,K \tag{1}$$

the area corresponding to that grid point was identified as desert or arid land. Figure 1 shows the results of this procedure over the area of interest. It is clear how the Sahara desert and the Arabian desert have been correctly identified as arid land. Smaller areas of arid land also appears in Iran (including the Dasht-e Kavir and the Dasht-e lut deserts) and in the African continent (including the Kalahari desert in South-West Africa and arid regions in the continental Horn of Africa). However some small deserts near to the coast have been not correctly identified, i.e. the Namib Desert in Namibia and the Danakil Desert in the African coast of the Red sea. The Coast pixels have been excluded from this test to eliminate the polarization difference due to the sea surface emissivity.

The differences in the observation geometry between SSMIS or AMSU/MHS and TRMM-PR creates spatial shifts in the retrieved rainfall patterns at the surface, and this is especially true for deep convective clouds. We considered this parallax error and partially corrected it by calculating the cloud top height (h) from the PR reflectivity profile (as the top PR reflectivity value larger than 0 dbZ) and then translating the PR surface rainfall rate in the direction of the observation of the radiometer by a distance ds defined as:

$$\text{ds } = h \tan(\theta) \tag{2}$$

where θ is the radiometer observation angle (fixed for SSMIS and variable for AMSU/MHS). The direction of the correction takes into account the angle α, i.e. the angle between PR and satellite orbit (projected to the earth surface) and the angle β, i.e. the orientation of the satellite orbit with respect to the Earth meridians. Figure 2 shows an example of two coincident observations of SSMIS and TRMM-PR and clarifies the meaning of the main variables involved in the calculation of the parallax error correction.

3 Methodology

In this work we have considered all channels of both datasets (AMSU/MHS and SSMIS) except the channels of the 50–60 GHz band with a peak of the weighting function too high for the scope of this work, i.e. we have excluded the channels in the 50–60 GHz band with a frequency higher than 55.5 GHz.

The first test that we performed was done in order to select the combination of channels that is more suitable to discriminate the signal deriving from the precipitating cloud ("rain") from the signal deriving from the background surface ("no rain"). We call this mono-dimensional combination of channels the discriminant function. In order to obtain and test different discriminant functions we have applied two well known multivariate methods: Empirical Orthogonal Function (EOF) analysis and Canonical Correlation Analysis (CCA) (Wilks, 1995). Both procedures consist of a projection of a multi-dimensional space (TBs) in a new set of coordinates, and, while the Principal Components (resulting from an EOF analysis) are ordered by the increasing variance, the Canonical Variables (resulting from a CCA) are ordered by the correlation with a third variable (in our case the surface rainfall rate). We have calculated 7 candidate discriminant functions and we tested them in a simple discriminant analysis test. The test consisted in applying 3 multivariate statistical procedures either on the part of the datasets (SSMIS and AMSU/MHS) with precipitating pixels ("rain"), or on the part of the datasets with not precipitating pixels ("no rain") (as observed by the TRMM-PR). The first procedure consisted in applying an EOF analysis on the TBs corresponding to "no rain" pixels, with the resulting combination of channels hereafter called PCA_N. Once the principal components were calculated we discarded the first components (linked mostly to the signal deriving from the surface), in order to obtain a set of independent components (combination of TBs) with minimum signal coming from the surface. A second procedure consisted in applying an EOF analysis on the TBs corresponding to "rain" pixels, obtaining combination of channels hereafter called PCA_R, and discarding the last components. A third procedure consisted in calculating the CCA on the "rain"

fraction of the dataset, in order to select the linear combination of TBs which has the maximum correlation with rain rate (CCA_R). The objective of these last two procedures was to enhance the signal emitted by precipitating clouds. In the work of (Petty, 2013) two of this procedures (PCA_N and PCA_R) were applied to a dataset of TBs in order to enhance the signal from precipitation and to mask the signal coming from the surface background. In this study we have tested 7 candidate discriminate functions consisting of different combinations of the 3 procedures described above (PCA_N, PCA_R and CCA_R). Table 1 shows a synthetic description of the 7 candidate discriminant functions.

The 7 candidate discriminant functions have been tested with a simple linear discriminant analysis (Wilks, 1995) in order to test the ability of each function to discriminate the "rain" and "no rain" pixels. First, the SSMIS dataset has been considered with a PR-based rain/no-rain threshold of $0.1\,\mathrm{mm\,h^{-1}}$ for each surface class. Then the same analysis was repeated for the AMSU/MHS dataset (for each surface class). The results in terms of Heidke Skill Score (HSS) (which measures the fractional improvements over random chance) for the SSMIS dataset are shown in Fig. 3. The HSS is defined as:

$$\mathrm{HSS} \ = \frac{2(hc - fm)}{(h + m)(m + c) + (h + f)(f + c)} \tag{3}$$

where h, m, f, and c are the fractional *hits*, *misses*, *false detections*, and *correct rejections* in a contingency table (Wilks, 1995). The *HSS* falls within a $[-\infty, +1]$ range, an HSS equal to 1 indicates the perfect score.

Looking to Fig. 3 it is clear how PCA_N and PCA_R have a relatively low skills over all background surfaces except for vegetated land. On the other hand CCA_R, PCA_R-CCA_R and PCA_N-PCA_R-CCA_R have the best skill score over all surfaces and behave quite similarly. Finally PCA_N-PCA_R and PCA_N-CCA_R have a skill variable depending on the surface type. CCA_R shows a high HSS and is a relatively simple procedure, being the result of a canonical correlation analysis on the TBs associated to rainfall as observed from the TRMM-PR. Similar results of the HSS were obtained for the ASMU/MHS dataset. From the results of this analysis we have chosen the CCA_R as the discriminant function of our novel algorithm for detection of precipitation.

The novel algorithm was trained using separately two datasets, the one of coincidences of SSMIS with PR and the one of coincidences of AMSU/MHS with PR, considering the full set of 2011–2012 observations. We have also tested how the novel detection algorithm would perform with a pseudo-GMI radiometer, by selecting only the channels from the SSMIS dataset more similar to those of the GMI radiometer (i.e., the SSMIS channels in the 50–60 GHz absorption band and at 183 ± 1 GHz were discarded).

The precipitation detection algorithm has been defined in two steps, for each of the three datasets (SSMIS-PR, AMSU/MHS-PR, and pseudo GMI-PR) and considering the four different background surface types. First, we have carried out the CCA_R (i.e., on the TBs of "rain" pixels) to find the coefficients (a_i) of the Canonical Variables (CV) (linear combination of TB channels best correlated to precipitation), defined as:

$$CV = \sum_{i=1}^{n} a_i \left(TB^i - \overline{TB}_R^i \right) \tag{4}$$

where the index i spans over the n available channels of the radiometer (SSMIS, AMSU/MHS, or pseudo-GMI), TB^i are the brightness temperatures in each pixel, and TB_m^i are the mean brightness temperatures over the full "rain" dataset. Then, we found the threshold value of CV to discriminate between "rain" and "no rain" pixels (CV_{th}). It was computed by analyzing the variability of HSS over the full dataset for different threshold values CV_{th} (ranging between -2 K and 8 K), using the TRMM-PR rainfall product as "truth" with minimum "rain" threshold of 0.1 mm h^{-1}. We have selected the threshold value CV_{th} which maximize the HSS; this procedure was repeated for each surface background and radiometer dataset. Therefore, for each surface and for each radiometer a set of coefficients a_i and a threshold value CV_{th} was determined to discriminate between "rain" and "no rain" pixels.

Full Screen / Esc

Printer-friendly Version

Interactive Discussion

The novel rain detection algorithm (from here on called CCA algorithm) marks as "rain" those pixels where:

$$CV = \sum_{i=1}^{n} a_i \left(TB^i - \overline{TB}_R^i \right) > CV_{th} \tag{5}$$

The resulting coefficient of the CCA_R analysis (a_i) and the chosen threshold CV_{th} are summarized in Appendix A for each radiometer (SSMIS, AMSU/MHS, or pseudo-GMI) and for each type of surface background.

4 Results

In the tuning of the algorithms we classified the precipitating pixels adopting an arbitrary rainfall rate threshold of $0.1\,\mathrm{mm\,h^{-1}}$; however it is possible that in some conditions the radiometric signal is not suited to detect such light precipitation. Moreover an algorithm for the detection of precipitation is always a compromise between the need of detecting the lower minimum threshold of rain rate and the requirement of low detection errors in terms of both false alarms and misses. In this Section (Fig. 4 and in Fig. 5) we analyze the results of the CCA algorithm for different rainfall rate thresholds (RR_{th}), using as ground truth for "rain" pixels TRMM-PR 2A25 product. We compare the results with those obtained from widely used screening algorithms (presented in Sect. 1) applying them on the same datasets used for the CCA algorithm. In particular, we have used 4 other different procedures: (1) following (Ferraro, 1997), hereafter *F97-SI*, we have calculated the scattering index (SI) over land and ocean considering also the estimated columnar water vapor from 19 GHz and 37 GHz over ocean; (2) following the Polarization Corrected Temperature (PCT) algorithm from (Spencer et al., 1989) (hereafter *SGH-PCT*) we have calculated the PCT with $\beta = 0.45$, considering as "rain" the pixels with $PCT < 255\,K$; (3) we have considered the AMSU/MHS screening algorithm from (Chen and Staelin, 2003), which considers differences between the 183 GHz channels

D. Casella et al.

and the 53.6 GHz and is applicable over each type of surface background considered in this study (hereafter *CS03*); (4) following the methodology developed by Grody and Weng (2008) and used by many authors (e.g. Laviola and Levizzani, 2009, 2011) we have considered the TB difference between the MHS channels at 89 GHz (or SSMIS and GMI-like 91.6 GHz) and 150 GHz as a simple mask in order to detect the scattering signal from precipitation (hereafter *GW08*). The "rain" threshold on this TB difference has been set to 5 K. Table 2 shows a synthetic description of the algorithms used for comparison in this study.

The results are shown in terms of HSS, Probability of Detection (POD) and False Alarm Ratio (FAR), defined as:

$$\text{POD} = \frac{h}{(h+m)}; \quad \text{FAR} = \frac{f}{(f+h)} \tag{6}$$

with the same reference to a contingency table used in Eq. (3).

Figures 4 and 5 show the results for the SSMIS (and pseudo-GMI) datasets and for the AMSU/MHS datasets respectively, for all types of surface background. All tested algorithms have higher POD for higher RR_{th} because high rain rates are *usually* associated to precipitating clouds with a strong radiometric signals (except in some cases such as warm rain over land). It is worth noting, however, that the impact on the TBs in the different microwave channels depends on several factors, such as the surface background, environmental and meteorological conditions, and the microphysical structure of the cloud. FAR grows with RR_{th} as well in all of the algorithms considered, as a consequence of the fact that by increasing RR_{th} the size of areas considered as precipitating by the TRMM-PR is reduced, while the areas identified as "rain" by the detection algorithms are unchanged. The overall performance of the detection algorithms can be evaluated by looking at the HSS (last row in each figure). It is interesting to look at the threshold RR_{th} that maximize the HSS and the corresponding HSS value for each type of algorithm.

In Fig. 4, over Arid Land the CCA algorithm applied to SSMIS and pseudo-GMI (CCA-SSMIS and CCA-GMI) shows a POD lower than the other algorithms (except for

SGH-PCT) but it also shows a very low FAR, which counterbalances the POD. This results in a HSS higher (i.e., better performance) of the CCA algorithm than for the other algorithms. The SGH-PCT shows a relatively low POD and a very low FAR over Arid Land (and to a less extent also over other types of surface background), and has higher HSS than CCA only for rain rates higher than $0.9\,\mathrm{mm\,h^{-1}}$. The major drawback of the SGH-PCT algorithm is that it needs to use both polarization of the SSMIS (or pseudo-GMI) 91 GHz channels, and, therefore, it is not applicable to AMSU/MHS or other cross-track scanning radiometers. It is also worth noting that the F97-SI algorithm is not suited for detecting precipitation over desert (Arid Land) because the use of the SI leads to the misclassification of the signal deriving from the surface as precipitation (in fact it was not applied to desert background in the original work by Ferraro, 1997). Over Vegetated Land the CCA-SSMIS and CCA-GMI algorithm performs very well, with high values of POD (between 0.6 and 0.8) and low values of FAR (between 0.2 and 0.5). Over Coast the CCA suffers from relatively low POD values. However the HSS skill score is higher than all other tested algorithms with the only exception of the SGH-PCT for $\mathrm{RR_{th}}$ higher than $1\,\mathrm{mm\,h^{-1}}$. Over ocean the CCA algorithms have higher POD than the others (while the FAR is comparable to CS-03, lower than GW08, and higher than F97-SI and SGH-PCT). Over ocean CCA-SSMIS and CCA-GMI show higher HSS than the other algorithms, except the F97-SI which has higher HSS for $\mathrm{RR_{th}}$ larger than $0.2\,\mathrm{mm\,h^{-1}}$. It is interesting to analyze the values of $\mathrm{RR_{th}}$ where the HSS is maximized. The CCA algorithm was set up by finding the $\mathrm{CV_{th}}$ that maximize the HSS for a $\mathrm{RR_{th}}$ of $0.1\,\mathrm{mm\,h^{-1}}$. However calculating the HSS with a variable $\mathrm{RR_{th}}$ we find in all cases a maximum HSS for $\mathrm{RR_{th}}$ higher than $0.1\,\mathrm{mm\,h^{-1}}$. The position and the score of the maximum HSS for a variable $\mathrm{RR_{th}}$ is related to the rain rate value that is best discriminated by the algorithm. The CCA algorithm maximize the HSS around $0.2\,\mathrm{mm\,h^{-1}}$ threshold over all surface background conditions except over coast. Over ocean F97-SI (with higher HSS than CCA for $\mathrm{RR_{th}}$ larger than $0.2\,\mathrm{mm\,h^{-1}}$) maximizes the HSS around $0.5\,\mathrm{mm\,h^{-1}}$. We can conclude that over ocean the CCA algorithm is more suitable to detect low precipitation rates ($\mathrm{RR_{th}} \leq 0.2\,\mathrm{mm\,h^{-1}}$) than the F97-

SI; however *F97-SI* is preferable to detect higher precipitation rates. The CCA-GMI algorithm behaves very similarly to the CCA-SSMIS in all situations.

Figure 5 shows that the CCA-AMSU has a behavior similar to the CCA-SSMIS (CCA-GMI). No results for *F97-SI* and *SGH-PCT* are presented in this figure because these two approaches can not be applied to the AMSU/MHS radiometers, since the 19 GHz channel and the two polarization of the 89 GHz are not available. Over desert (Arid Land) the CCA-AMSU performs better than the other algorithms (higher HSS, due to the significantly lower FAR), but the absolute value of FAR is still quite high (between 0.5 and 0.7) and higher than for CCA-SSMIS. Over Land the skill of the CCA-AMSU algorithm is higher than for the other algorithms, and it is quite similar to the CCA-SSMIS algorithm but slightly worse (due to the higher FAR). Over Coast the CCA-AMSU has higher skill score for RR_{th} lower than $0.5\,\text{mm}\,\text{h}^{-1}$, but the *GW08* has significantly better scores for higher values of RR_{th}. Over Ocean the *CS03* algorithm seems to work better (in terms of HSS) than the CCA-AMSU for higher values of RR_{th}, with maximum HSS reached at $0.2\,\text{mm}\,\text{h}^{-1}$ and at $0.6\,\text{mm}\,\text{h}^{-1}$ for the CCA-AMSU and for the *CS03* respectively.

In summary, the results in Figs. 4 and 5 show the ability of the CCA screening algorithm to discriminate between precipitation greater or lower than a given rain rate threshold, in terms of detection efficiency and false alarms, and overall show better skills than the other algorithms in particular in terms of lower FAR in all conditions with the exception of SSMIS and GMI over ocean. In this conditions the *F97-SI* performs better, at least for precipitation rates higher than $2\,\text{mm}\,\text{h}^{-1}$. The algorithm has been trained and optimized (in terms of HSS) to detect rain rates larger than $0.1\,\text{mm}\,\text{h}^{-1}$. However, the HSS reaches the maximum value for RR_{th} higher than $0.1\,\text{mm}\,\text{h}^{-1}$, indicating that the algorithm performs even better for higher rain/no-rain threshold values.

We now want to verify how well the CCA algorithm is able to cathegorize "no rain" pixels and what is the rainfall intensity associated with misclassified pixels. Figure 6 shows the results of a binning technique (following Ferraro and Marks, 1995) applied to the TRMM-PR rainfall rate corresponding to the CV values (Eq. 4) of each pixel. For

Title Page

Abstract | Introduction

Conclusions | References

Tables | Figures

|◄ | ►|

◄ | ►

Back | Close

Full Screen / Esc

Printer-friendly Version

Interactive Discussion

each dataset (i.e., for SSMIS, AMSU and pseudo-GMI and for four different type of surfaces) the CV range of values has been divided into bins 0.2 K wide, and the mean and the standard deviation of the TRMM-PR rainfall rate corresponding to each CV value, has been calculated for each bin. Each panel shows the trend of the mean rainfall rate (and standard deviation) with the CV binned values. A thick vertical dashed line represent the CV threshold chosen for each radiometer and surface background type as a result of the CCA training (i.e, CV_{th} in Eq. (5), Sect. 3; the values are also provided in Appendix A). Looking at the trend of mean rain rate with CV and at the rain rate standard deviation it is evident that increasing values of CV are on average associated with increasing values of rainfall rate. All the pixels falling in the bins below CV_{th} are misclassified as "no rain" and they correspond to the low rainfall values (below $0.5\,mm\,h^{-1}$ for all the datasets). We have considered the minimum detectable rainfall rate for each dataset (RR_b) as the mean value corresponding to the CV_{th}. In Appendix A the values of RR_b are reported and the scores of the CCA algorithm based on these thresholds are also provided. It is clear from Fig. 6 and Table 3 how the CCA performs better over Vegetated Land and Ocean for both SSMIS and AMSU, and RR_b is lower over Ocean (less than $0.2\,mm\,h^{-1}$) and higher over land (around $0.3\,mm\,h^{-1}$). Over Arid Land it is possible to discriminate lower value of rain intensity (around $0.23\,mm\,h^{-1}$) but the strong variability in the surface emissivity brings to a higher ratio of misses (lower POD). Over Coast the results are quite different between the SSMIS and the AMSU algorithms, as for SSMIS there is a good correlation between the mean rain rate and the CV values with a large spread, while the AMSU shows smaller spread with a more irregular trend of the mean rain rate value. The RR_b over Coast for the SSMIS is the highest among all the datasets ($0.40\,mm\,h^{-1}$), while the irregular trend of the mean rain rate over coast for the AMSU algorithm makes the RR_b over coast ($0.18\,mm\,h^{-1}$) uncertain. As far as the pseudo-GMI dataset, it is worth noting that it was generated from the SSMIS dataset only by discarding the channels not available in the GMI radiometer. Therefore it can be representative of the performance of a CCA algorithm for the real GMI radiometer only to a certain extent, considering only the instrument ob-

Title Page

Abstract | Introduction

Conclusions | References

Tables | Figures

|◄ | ►|

◄ | ►

Back | Close

Full Screen / Esc

Printer-friendly Version

Interactive Discussion

servation geometry (conical scanning) and the channels frequencies and polarizations, with the exclusion of the 10 GHz channels (not available on SSMIS) which might have a significant impact on precipitation detection over ocean. Moreover, the differences in the resolution of the GMI and SSMIS sensors have not been considered, and this may strongly affect the results. The results of the binning technique for the pseudo-GMI dataset show some differences with respect to the SSMIS both in terms of mean rain rate and standard deviation. Moreover the RR_{th} is lower over Land (Vegetated and Arid) and Coast and higher over Ocean. The statistical scores in Table 3 show some differences as well, with HSS generally lower than for SSMIS over all surface types except Coast (which shows an increase of the performance of the algorithm in terms of POD).

The probability density function of rainfall rate over a long period has been described as a gamma or a lognormal distribution with a mode near $0\,mm\,h^{-1}$, therefore low values of rain rate are more probable then high values (Cho et al., 2004). Moreover we have seen from results shown in Figs. 4 and 5 that all the algorithms considered detect more efficiently high rain rates than low rain rates. (POD increasing with rain rate.) As a consequence the probability of missing the low precipitation may be very high using this kind of algorithms with a strong impact on the estimate of the total precipitation. This is probably the main reason why many authors are more interested in developing detection algorithms with high sensitivity (high POD) than with high specificity (low FAR). However the choice of the best detection algorithm depends on many factors and on the application. For example, the ability to reduce false alarms becomes important when precipitation is a rare event as in arid areas, and where drought monitoring is a priority. Therefore, when a screening procedure is applied in a precipitation retrieval, it is important not only to evaluate the total precipitation correctly detected or missed, but it is also essential to differentiate and evaluate the impact of false alarms.

We want here to estimate the impact of different detection algorithm on the total precipitation estimate. In order to do so we delineate a "perfectly" working estimate algorithm that always estimates the ground truth whenever precipitation is detected

Title Page

Abstract | Introduction

Conclusions | References

Tables | Figures

Back | Close

Full Screen / Esc

Printer-friendly Version

Interactive Discussion

(also in case of false alarm). In case of a false alarm we assume that our "perfect" algorithm output will be the mean value of precipitation rate over the full dataset ($\overline{rr}$) (i.e. $0.68\,\text{mm}\,\text{h}^{-1}$ and $0.47\,\text{mm}\,\text{h}^{-1}$ for the SSMIS and AMSU datasets respectively). The fraction of precipitation due to hits (FPH) will be:

$$\text{FPH} = \frac{\sum_i (\text{rr}_i \cdot h_i) \cdot \Delta t}{\sum_i \text{rr}_i \cdot \Delta t} \tag{7}$$

where rr_i is the ground truth reference value of rainfall rate for a given observation (i), h_i is the hit state (i.e. it is equal to 1 if the observation i is a hit in a standard contingency table and it is equal to 0 otherwise) and Δt is the integration time. The fraction of precipitation due to false alarm (FPF) of the total precipitation will be:

$$\text{FPF} = \frac{\sum_i (\overline{rr} \cdot f_i) \cdot \Delta t}{\sum_i \text{rr}_i \cdot \Delta t} \tag{8}$$

where f_i is the false alarm state, with a definition equivalent to the hit state.

Figure 7 shows the results of this test for all the algorithm considered in this study. Over Arid Land the CCA algorithms can detect a relatively large fraction of the total precipitation (FPH 75–68 %) in comparison with the other algorithms considered, and shows a very low value of FPF. Over Vegetated land every algorithm considered detects a very high fraction of the precipitation (more than 80 % for the SSMIS and around 79 % for the AMSU) with the exception of *SGH-PCT*, but the CCA algorithm shows lower FPF. Over coast the CCA-SSMIS algorithm shows a FPH similar to the other algorithms but with a lower FPF; conversely the CCA-AMSU has higher FPH but also higher FPF. Finally over ocean the choice of the best algorithm depends on the kind of application: the CCA algorithms shows a higher FPH but also higher FPF than *F97-SI* (*CS03*) for SSMIS (AMSU). Ultimately the CCA algorithm behaves fairly well and have often FPH higher than 80 % with low values of FPF.

5 Conclusions

The CCA algorithm for the detection of precipitation described in this paper results from the application of two main procedures: (1) application of the canonical correlation analysis to a large dataset of coincident PMW multichannel observations and rainfall rate high quality estimates to define canonical variables for different types of surface background; (2) estimation of a threshold value for the canonical variables that maximize the Heidke Skill Score for a given rainfall rate threshold. The algorithm has been applied to three large datasets (SSMIS-PR, AMSU/MHS-PR and pseudo-GMI-PR), for four different types of surface background, and results have been compared to other well-known screening algorithms. The resulting CCA algorithm is simple, and it can be adapted to any other PMW radiometer, and to any other geographical region where a large dataset of coincident precipitation measurements and PMW observations from that radiometer is available.

It is worth noting that the pseudo-GMI dataset was generated selecting the channels available in the GMI radiometer from the SSMIS dataset. Therefore the results from the pseudo-GMI dataset need to be looked at with some caution. The geometry of observation of the two instruments is very similar and the polarization and frequency of the selected channels almost coincide. However the pseudo-GMI dataset does not include the 10 GHz channels (that may be crucial over ocean) and the differences in the channels resolution may strongly affect the results.

The CCA algorithm shows almost always better performance in comparison with other well known algorithms especially in terms of low false alarm ratios. The HSS is always higher than all other algorithms tested except for AMSU/MHS over ocean or coast at large rainfall rate thresholds (> 0.4 and $0.6 \, \mathrm{mm \, h^{-1}}$ respectively) and for SSMIS over ocean for rainfall rate thresholds $> 0.2 \, \mathrm{mm \, h^{-1}}$. The estimate of the minimum rain rate that is efficiently detected by the algorithm shows values varying from $0.15 \, \mathrm{mm \, h^{-1}}$ (AMSU over ocean) to 0.40 (SSMIS over Coast) with the remarkable result of $0.23 \, \mathrm{mm \, h^{-1}}$ over Arid Land surface.

Due to the fact that light precipitation is usually more common than intense precipitation most algorithms for precipitation detection are set up to increase the sensitivity reducing the number of misses in the light precipitation. However in many conditions when the background surface signal may be confused with precipitation the number of false alarms may be very high. The CCA algorithm seems to perform well with both a good detection capability and low false alarm ratios in comparison with the other widely used algorithms analyzed in this paper. Therefore, it can be useful even when the occurrence of precipitation is rare, i.e. for drought monitoring. The total amount of precipitation that this algorithm can detect is around 80 % over Ocean and Vegetated land and between 68 and 75 % over Coast and Arid Land with a relatively low rate of false alarms (below 10 % for the SSMIS and below 15 % for the AMSU over Vegetated and Arid Land, and Coast).

The advent of the GPM era requires the combined use of different PMW radiometers with different channels and dissimilar observation geometry for global precipitation monitoring. This poses a difficult challenge to the scientific community, i.e., obtaining coherent estimates of precipitation from this constellation of radiometers. Lots of efforts are put into achieving consistency between precipitation pattern and precipitation estimates from the different sensors. Some fundamental improvements in this direction will come from the use of a common algorithm for the screening of non precipitating scenes applicable to all types of background surfaces. The CCA algorithm is an important step toward this goal, considering that it is suitable to be applied to any PMW sensor (conical and cross-track scanning) for which a long series of data coincidences with rainfall rate ground truth is available. In the EUMETSAT H-SAF project the consistency in the precipitation estimates between cross-track and conical scanning radiometers has been strongly improved by the use a common procedure for the detection of the precipitating clouds (besides the use of the same physical foundation in the retrieval algorithms; see Mugnai et al., 2013b; Panegrossi et al., 2013).

In the near future we plan to develop the algorithm for GMI, GCOM-W1 AMSR2 and Suomi-NPP ATMS. We are planning to take advantage of the imminent availability of

Title Page

Abstract | Introduction

Conclusions | References

Tables | Figures

|◀ | ▶|

◀ | ▶

Back | Close

Full Screen / Esc

Printer-friendly Version

Interactive Discussion

the GPM DPR products in order to extend and test the CCA procedure between 65° N and 65° S, especially over snow and ice covered surfaces. Moreover the estimates of the CloudSat Precipitation Radar may be used as ground truth (especially for snowfall and light precipitation) in order to create an even larger dataset of coincident obser-
vations of active and passive MW satellite borne instruments and extend the CCA algorithm to higher latitudes and to the polar regions.

Appendix A

Tables A1–3 show the CV thresholds (CV_{th}), the coefficients and mean TB values used by the CCA algorithms for the SSMIS, pseudo-GMI and AMSU/MHS datasets. The
mean TBs in the pseudo-GMI dataset are identical to the corresponding channels of the SSMIS dataset.

References

Barrett, E. C., Kidd, C., and Bailey, J. O.: A new instrument with rainfall monitoring potential, Int. J. Remote Sens., 9, 1943–1950, 1988.

Bennartz, R.: Optimal convolution of amsu-b to amsu-a, J. Atmos. Ocean. Tech., 17, 1215–1225, 2000.

Casella, D., Panegrossi, G., Sano, P., Dietrich, S., Mugnai, A., Smith, E. A., Tripoli, G. J., Formenton, M., Di Paola, F., and Leung, W.-Y.: Transitioning from CRD to CDRD in Bayesian retrieval of rainfall from satellite passive microwave measurements: Part 2. Overcoming database profile selection ambiguity by consideration of meteorological control on microphysics, IEEE T. Geosci. Remote, 51, 4650–4671, 2013.

Chen, F. W. and Staelin, D. H.: Airs/amsu/hsb precipitation estimates, IEEE T. Geosci. Remote, 41, 410–417, 2003.

Cho, H.-K., Bowman, K. P., and North, G. R.: A comparison of gamma and lognormal distributions for characterizing satellite rain rates from the tropical rainfall measuring mission, J. Appl. Meteorol., 43, 1586–1597, doi:10.1175/jam2165.1, 2004.

Desbois, M., Roca, R., Eymar L., Viltard, N., Viollier, M., Srinivasan, J., and Narayanan, S.: The Megha-Tropiques mission. Atmospheric and Oceanic Processes, Dynamics, and Climate Change, editd by: Sun, Z., Jin, F.-F., and Iwasaki, T., International Society for Optical Engineering, SPIE P., 4899, 172–183, doi:10.1117/12.466703, 2003

Edward, P., and D. Pawlak: MetOp: The space segment for EUMETSAT's polar system, ESA Bull., 102, 6–18, 2000.

Ferraro, R. R.: Special sensor microwave imager derived global rainfall estimates for climatological applications, J. Geophys. Res.-Atmos., 102, 16715–16735, doi:10.1029/97jd01210, 1997.

Ferraro, R. R. and Marks, G. F.: The development of SSM I^{-1} rain-rate retrieval algorithms using ground-based radar measurements, J. Atmos. Ocean. Tech., 12, 755–770, 1995.

GPM: Algorithm Theoretical Basis Document, NASA, available at: http://pmm.nasa.gov/sites/default/files/document_files/GPROF_ATBD_1Dec2010.pdf (last access: 7 September 2014), 2010.

Grecu, M. and Anagnostou, E. N.: Overland precipitation estimation from TRMM passive microwave observations, J. Appl. Meteorol., 40, 1367–1380, 2001.

Grody, N. C.: Classification of snow cover and precipitation using the Special Sensor Microwave Imager, J. Geophys. Res.-Atmos. (1984–2012), 96, 7423–7435, 1991.

Grody, N. C. and Weng, F.: Microwave emission and scattering from deserts: theory compared with satellite measurements, IEEE T. Geosci. Remote, 46, 361–375, 2008.

Hou, A. Y., Kakar, R. K., Neeck, S., Azarbarzin, A. A., Kummerow, C. D., Kojima, M., Oki, R., Nakamura, K., and Iguchi, T.: The global precipitation measurement mission, B. Am. Meteorol. Soc., 95, 701–722, doi:10.1175/BAMS-D-13-00164.1, 2014

Islam, T., Rico-Ramirez, M. A., Srivastava, P. K., and Dai, Q.: Non-parametric rain no-rain screening method for satellite-borne passive microwave radiometers at 19–85 GHz channels with the Random Forests algorithm, Int. J. Remote Sens., 35, 3254–3267, 2014.

Kummerow, C. D., Hong, Y., Olson, W., Yang, S., Adler, R., McCollum, J., Ferraro, R., Petty, G., Shin, D.-B., and Wilheit, T.: The evolution of the Goddard profiling algorithm (GPROF) for rainfall estimation from passive microwave sensors, J. Appl. Meteorol., 40, 1801–1820, doi10.1175/1520-0450(2001)040<1801:TEOTGP>2.0.CO;2, 2001.

A novel algorithm for detection of precipitation in tropical regions

D. Casella et al.

Title Page

Abstract	Introduction
Conclusions	References
Tables	Figures

|◀ | ▶|
◀ | ▶

Back | Close

Full Screen / Esc

Printer-friendly Version

Interactive Discussion

Kummerow, C. D., Ringerud, S., Crook, J., Randel, D., and Berg, W.: An observationally generated a priori database for microwave rainfall retrievals, J. Atmos. Ocean. Tech., 28, 113–130, 2011.

Kunkee, D. B., Poe, G. A., Boucher, D. J., Swadley, S. D., Hong, Y., Wessel, J. E., and Uliana, E. A.: Design and evaluation of the first special Sensor Microwave Imager/Sounder, IEEE T. Geosci. Remote, 46, 863–883, doi:10.1109/tgrs.2008.917980, 2008.

Laviola, S. and Levizzani, V.: Observing precipitation by means of water vapor absor tion lines: a first check of the retrieval capabilities of p the 183-WSL rain retrieval method, Riv. Ital. Telerilevam., 41, 39–49, 2009.

Laviola, S. and Levizzani, V.: The 183-WSL fast rain rate retrieval algorithm: Part I: Retrieval design, Atmos. Res., 99, 443–461, 2011.

Mugnai, A., Casella, D., Cattani, E., Dietrich, S., Laviola, S., Levizzani, V., Panegrossi, G., Petracca, M., Sanò, P., Di Paola, F., Biron, D., De Leonibus, L., Melfi, D., Rosci, P., Vocino, A., Zauli, F., Pagliara, P., Puca, S., Rinollo, A., Milani, L., Porcù, F., and Gattari, F.: Precipitation products from the hydrology SAF, Nat. Hazards Earth Syst. Sci., 13, 1959–1981, doi:10.5194/nhess-13-1959-2013, 2013a.

Mugnai, A., Smith, E. A., Tripoli, G. J., Bizzarri, B., Casella, D., Dietrich, S., Di Paola, F., Panegrossi, G., and Sanò, P.: CDRD and PNPR satellite passive microwave precipitation retrieval algorithms: EuroTRMM/EURAINSAT origins and H-SAF operations, Nat. Hazards Earth Syst. Sci., 13, 887–912, doi:10.5194/nhess-13-887-2013, 2013b.

Munchak, S. J. and Skofronick-Jackson, G.: Evaluation of precipitation detection over various surfaces from passive microwave imagers and sounders, Atmos. Res., 131, 81–94, 2013.

Muth, C., Webb, W. A., Atwood, W., and Lee, P.: Advanced technology microwave sounder on the National Polar-Orbiting Operational Environmental Satellite System, Geoscience and Remote Sensing Symposium, 2005. IGARSS '05. Proceedings. 2005 IEEE International, 1, 4 pp., 25–29 July 2005, doi:10.1109/IGARSS.2005.1526113, 2005.

Panegrossi, G., Sanò, P., Casella, D., Dietrich, S., Petracca, M., and Mugnai, A.: The H-SAF Passive Microwave Precipitation Retrieval Algorithms: a Verification Study Over Europe, EGU General Assembly Conference Abstracts, 12648, 2013.

Petty, G. W.: Dimensionality reduction in Bayesian estimation algorithms, Atmos. Meas. Tech., 6, 2267–2276, doi:10.5194/amt-6-2267-2013, 2013.

Sanò, P., Casella, D., Mugnai, A., Schiavon, G., Smith, E. A., and Tripoli, G. J.: Transitioning from CRD to CDRD in Bayesian retrieval of rainfall from satellite passive microwave measure-

ments: Part 1. Algorithm description and testing, IEEE T. Geosci. Remote, 51, 4119–4143, 2013.

Sanò, P., Casella, D., Panegrossi, G., Di Paola, F., Milani, L., Mugnai, A., Petracca, M., and Dietrich, S.: The Passive microwave Neural network Precipitation Retrieval (PNPR) algorithm for AMSU/MHS observations: description and application to European case studies, Atmos. Meas. Tech., in press, 2014.

Seto, S., Takahashi, N., and Iguchi, T.: Rain/no-rain classification methods for microwave radiometer observations over land using statistical information for brightness temperatures under no-rain conditions, J. Appl. Meteorol., 44, 1243–1259, doi:10.1175/JAM2263.1, 2005.

Shimoda, H.: GCOM missions. Proc. IGARSS'05, Vol. 6, IEEE, Seoul, South Korea, 4201–4204, 2005

Spencer, R. W., Goodman, H. M., and Hood, R. E.: Precipitation retrieval over land and ocean with the SSM/I: identification and characteristics of the scattering signal, J. Atmos. Ocean. Tech., 6, 254–273, 1989.

Wilheit, T. T.: Comparing calibrations of similar conically scanning window-channel microwave radiometers, IEEE T. Geosci. Remote, 51, 1453–1464, 2013.

Table 1. Description of the 7 candidate discriminant functions.

	Discriminant Function	Short description	Comments/Goal
1	PCA_N	EOF analysis on "no rain" pixels – 1st component chosen	To enhance the signal from the background surface
2	PCA_R	EOF analysis on "rain" pixels – 1st component chosen	To enhance the signal from precipitation.
3	PCA_N-PCA_R	EOF analysis on "no rain" observations, discarding the first 3 components, and EOF analysis on "rain" pixels selecting the 1st component	To mask the background signal and enhance the signal from precipitation following Petty (2013)
4	CCA_R	CCA of TB's for "rain" pixels – 1st canonical variable	To enhance the signal from rain.
5	PCA_N-CCA_R	As in row 3, with the difference that the second procedure is a CCA of TB's for "rain" pixels	Same goal as row 3, with change from Petty (2013) in the second step.
6	PCA_R-CCA_R	(1) EOF analysis on "rain" pixels – discarding the last 3 components. (2) CCA application to the selected components – 1st canonical variable	Same goal as row 3. As suggested by Wilks (1995) CCA is supposed to be more stable if applied to selected components (eliminating those more affected by random noise).
7	PCA_N-PCA_R-CCA_R	As in row 3 with one more step (as row 6): a CCA is applied to the PCA_R after the last 3 components are discarded	To mask the background signal and enhance the signal from precipitation, joining row 6 and row 3 procedures.

Table 2. Algorithms used for comparison in the study. (*) Used only for SSMIS and pseudo-GMI datasets.

Acronym	Brief Description	Reference
F97-SI (*)	Scattering index (SI) over land and ocean using 19 GHz and 22 GHz and estimated IWV over ocean using 37 GHz.	Ferraro (JGR, 1997)
SGH-PCT (*)	Polarization Corrected Temperature (PCT) algorithm; we have calculated the PCT with $\beta = 0.45$, considering as "rain" the pixels with PCT < 255 K	Spencer et al. (JAOT, 1989)
CS03	Considers differences between the 183 GHz channels and the 53.6 GHz and is applicable over each type of surface background considered in this study	Chen and Staelin (TGRS, 2003)
GW08	TB difference between the MHS channel at 89 GHz (or 91.6 GHz for SSMIS and pseudo-GMI) and 150 GHz to detect the scattering signal from precipitation	Grody and Weng (TGRS, 2008)

Table 3. Value of the mean rain rate corresponding to the CCA threshold set for every combination of radiometer and surface background.

	SSMIS				AMSU/MHS				GMI			
	Arid Land	Veg. Land	Coast	Ocean	Arid Land	Veg. Land	Coast	Ocean	Arid Land	Veg. Land	Coast	Ocean
RR_{th} (mm h^{-1})	0.23	0.29	0.40	0.18	0.23	0.33	0.18	0.15	0.18	0.28	0.29	0.35
POD (RR_{th})	0.57	0.70	0.53	0.59	0.53	0.69	0.55	0.63	0.59	0.57	0.69	0.51
FAR (RR_{th})	0.46	0.43	0.42	0.46	0.61	0.51	0.59	0.53	0.47	0.42	0.44	0.44
HSS (RR_{th})	0.55	0.60	0.53	0.53	0.45	0.53	0.40	0.49	0.53	0.57	0.59	0.51

Table A1. List of CCA coefficient and CV_{th} threshold used by the CCA algorithms for the SSMIS radiometer.

ch. #	SSMIS CV_{th} ch. Name [GHz]	Arid Land 2.0 K		Vegetated Land 0.7 K		Coast 1.1 K		Ocean 0.8 K	
		a	TB_m	a	TB_m	a	TB_m	a	TB_m
1	150	0.00	274.40	0.00	276.73	0.00	276.61	0.00	276.30
2	183 ± 6.6	−0.10	272.48	−0.02	267.56	−0.03	270.68	0.00	271.91
3	183 ± 3	0.00	263.14	0.00	259.80	0.01	262.49	0.00	263.61
4	183 ± 1	0.03	249.42	0.00	246.65	0.01	249.05	0.01	249.34
5	91.6 V	−0.07	280.82	−0.13	281.01	−0.18	274.14	−0.20	266.01
6	91.6 H	−0.03	268.83	0.05	278.34	0.06	258.28	0.06	240.68
7	19 H	0.05	260.85	0.01	278.44	0.01	211.03	−0.03	144.35
8	19 V	−0.17	290.94	0.06	284.38	−0.05	246.79	0.24	205.20
9	22.2 V	0.27	290.47	0.13	285.54	0.04	263.35	−0.08	237.36
10	37 H	−0.02	263.03	−0.02	276.9	−0.04	219.65	−0.03	164.38
11	37 V	0.00	285.96	−0.10	281.04	0.09	251.8	0.07	220.01
12	50.3	0.02	274.53	0.01	275.61	0.01	261.51	−0.01	247.48
13	52.8	−0.10	265.65	−0.11	265.00	−0.06	263.92	0.01	261.96
14	53.6	0.08	249.91	0.06	249.93	0.10	249.88	0.02	249.34
15	54.4	0.01	220.88	0.00	220.93	0.01	220.07	0.01	220.44
16	55.5	−0.02	211.12	−0.03	210.08	−0.03	210.69	0.00	211.01

Table A2. List of CCA coefficient and CV_{th} threshold used by the CCA algorithms for the pseudo-GMI dataset.

ch. #	GMI ch. Name [GHz]	Arid Land 2.1 K a	Vegetated Land 0.7 K a	Coast 1.1 K A	Ocean 0.8 K a
1	150	0.00	0.00	0.00	0.00
2	183 ± 6.6	−0.11	−0.02	−0.03	0.01
3	183 ± 3	0.03	0.01	0.02	0.00
5	91.6 V	−0.08	−0.14	−0.19	−0.21
6	91.6 H	−0.02	0.06	0.06	0.06
7	19 H	0.05	0.01	0.01	0.00
8	19 V	−0.18	0.08	−0.06	0.20
9	22.2 V	0.28	0.11	0.05	−0.07
10	37 H	−0.02	−0.02	−0.04	−0.05
11	37 V	0.00	−0.11	0.10	0.09

Title Page

Abstract | Introduction

Conclusions | References

Tables | Figures

◄ | ►

Back | Close

Full Screen / Esc

Printer-friendly Version

Interactive Discussion

Table A3. List of CCA coefficient and CV_{th} threshold used by the CCA algorithms for the AMSU/MHS dataset.

	AMSU A -MHS CV_{th}	Arid Land 2.4 K		Vegetated Land 0.6 K		Coast 0.8 K		Ocean 0.6 K	
ch. #	ch. Name [GHz]	a	TB_m	a	TB_m	a	TB_m	a	TB_m
1	89	0.07	231.00	0.17	277.12	0.07	279.39	0.03	253.55
2	150	−0.05	270.72	−0.15	278.22	−0.07	278.67	−0.08	269.09
3	183.3 ± 1	0.01	245.48	0.07	247.08	0.03	245.32	0.06	238.48
4	183.3 ± 3	0.05	258.51	0.02	260.36	0.06	257.96	0.06	251.25
5	183.3 ± 7	−0.08	267.58	−0.11	271.99	−0.09	267.43	−0.07	260.87
6	23.8	−0.05	186.65	0.27	285.71	0.20	282.44	0.07	242.39
7	31.4	0.20	165.92	−0.26	284.17	−0.07	279.96	−0.05	230.58
8	50.3	−0.29	230.79	−0.10	284.83	−0.27	280.53	0.00	260.37
9	52.8	0.13	261.44	0.12	276.41	0.15	272.25	−0.12	269.79
10	53.6	−0.11	256.34	−0.10	261.16	−0.03	258.04	−0.15	259.44
11	54.4	0.02	238.66	0.10	240.45	0.04	238.18	0.35	240.40
12	54.9	0.17	228.55	−0.10	230.14	−0.05	227.77	−0.09	230.09
13	55.5	−0.08	215.23	0.02	216.91	0.03	214.16	−0.10	216.59
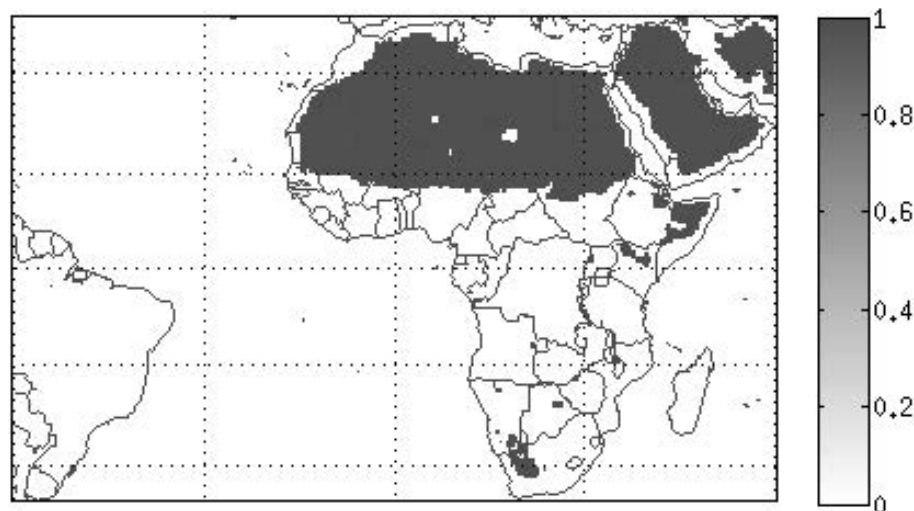
Figure 1. Map of Arid Land identified using the annual mean of the 19 GHz channels difference (V − H). Dark grey areas are the regions identified as desert or arid land.
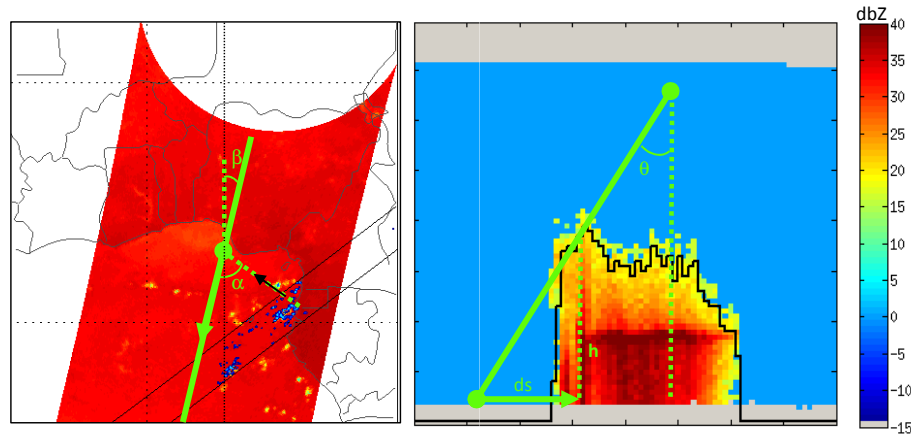
Figure 2. Example of parallax correction. Left panel shows the superposition of a section of SSMIS orbit 91 H channel TB and the coincident TRMM-PR rainfall rate (in blue contour). The angles α and β are defined (see text for details) the direction of the correction is shown as a black arrow, right panel shows the vertical section of the reflectivity as measured by the TRMM PR, a black line shows the cloud top height for the full section, the quantities θ, ds and h are defined (see text for details).
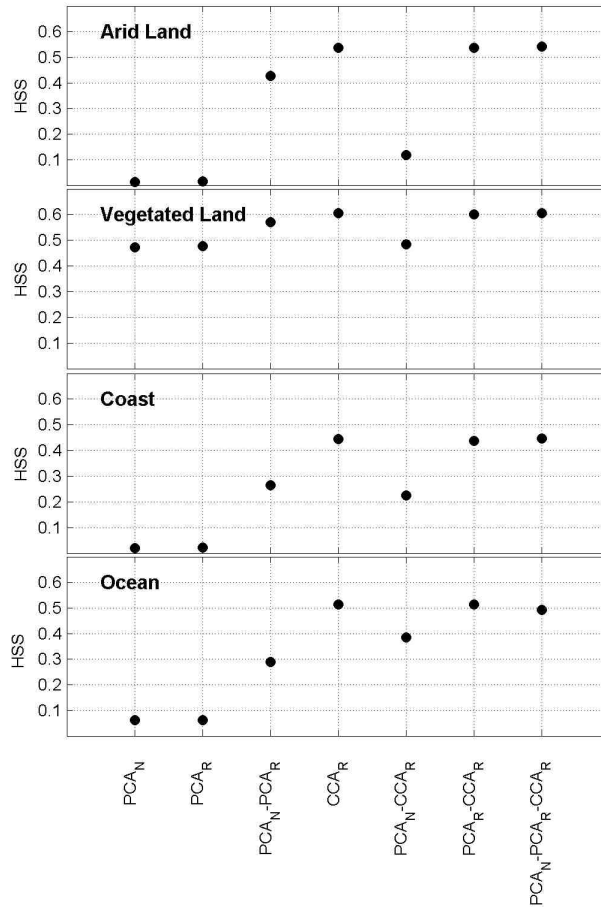
Figure 3. Results of the choice of the discriminant function over different background surface for the SSMIS dataset, the labels of the x-axis identify the discriminant function used (see text for details) and the value represented in the y-axis is the Hedke Skill Score.

Full Screen / Esc

Printer-friendly Version

Interactive Discussion
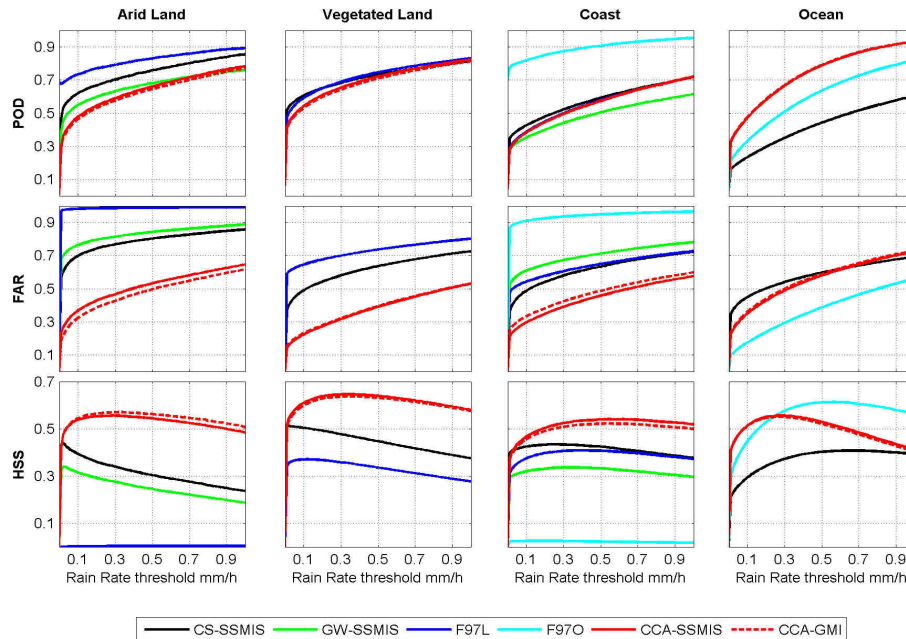
Figure 4. Comparison of the CCA-SSMIS and CCA-GMI algorithm with other similar algorithm for the detection of precipitation using as ground truth for the precipitating pixels the PR-rain rate with a variable threshold (represented in the x-axis). The results are summarized in 4 column of panels (one for each surface background) in terms of POD (upper line of panels), FAR (middle) and HSS (lower panels). The scales are the same for every plot.
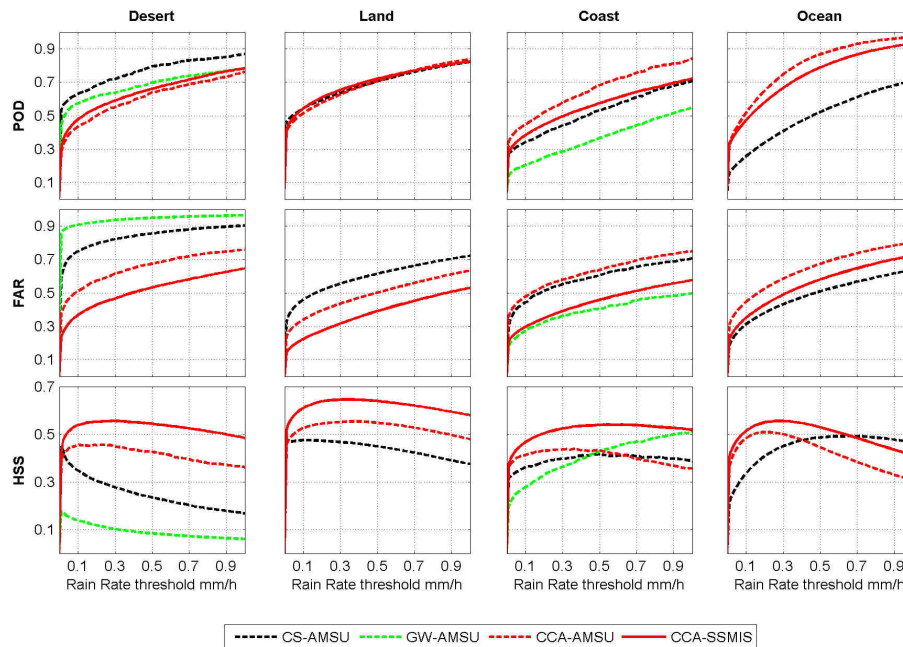
Figure 5. Equivalent to Fig. 4 for the AMSU/MHS dataset, CCA-SSMIS (red solid curve) represents the results of the CCA algorithm applied to SSMIS dataset (same results of Fig. 4) and are shown here for comparison.
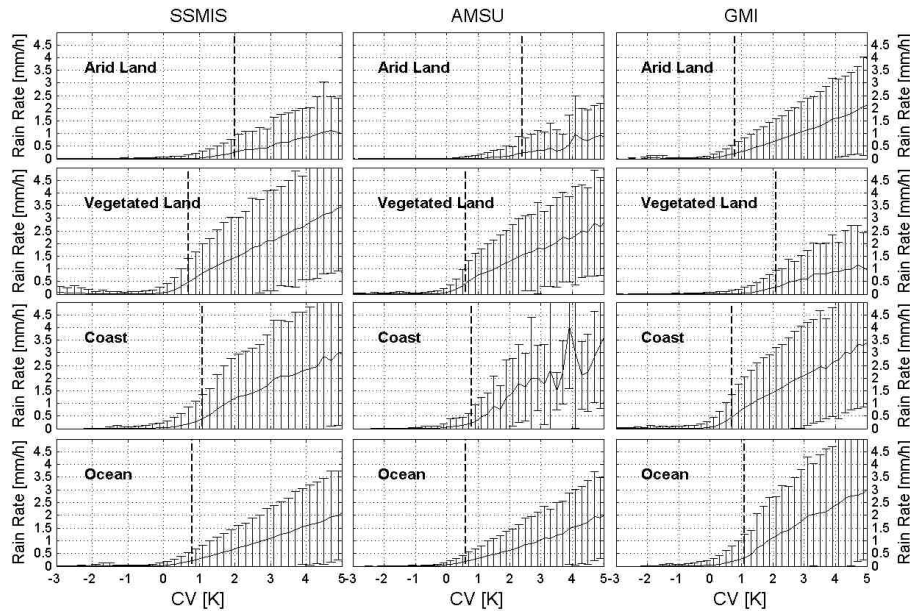
Figure 6. Binning analysis of the Rain rate intensity against CV values: mean (continuous black line) and standard deviation (error bars) of rain rates inside an interval of CV bins (as large as 0.2 K) are shown. He vertical dashed line represents the CV threshold (CVth) chosen for each combination of radiometer and surface background.
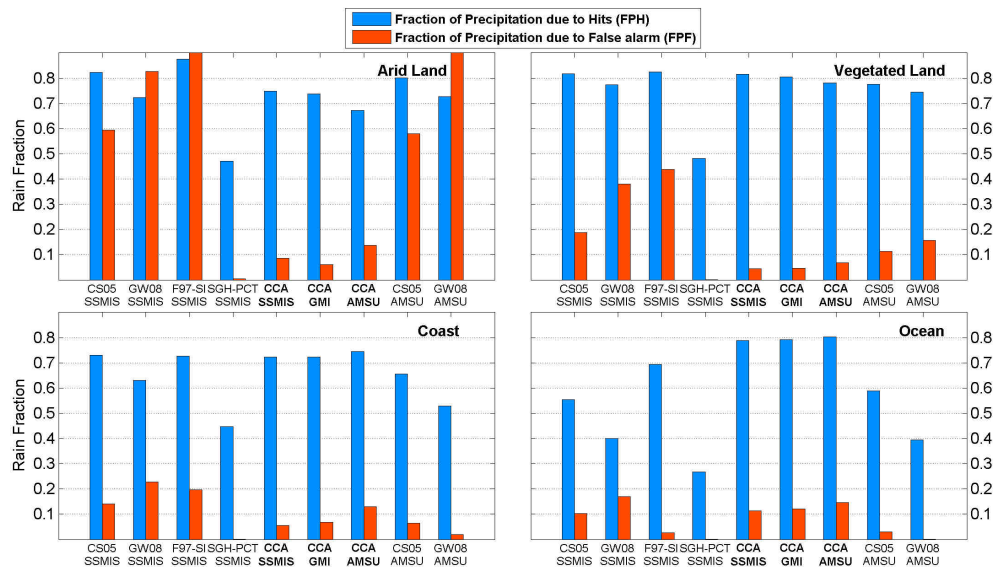
Figure 7. Evaluation of the total error on the precipitation estimate for the various algorithm considered.